

Magnetic Effects at the Edge of the Solar System: MHD Instabilities, the *de Laval* nozzle Effect and an Extended Jet

M. Opher¹ and P. C. Liewer¹

Jet Propulsion Laboratory, MS 169-506, 4800 Oak Grove Drive, Pasadena, CA 91109

merav.opher@jpl.nasa.gov

M. Velli^{1,2}, L. Bettarini²

Departament of Astronomy and Space Science, Univ. of Firenze, Firenze, IT 50125

T. I. Gombosi³, W. Manchester³, D. L. DeZeeuw³, G. Toth³ and I. Sokolov³

Space Physics Research Laboratory, Department of Atmospheric, Ann Arbor, MI

ABSTRACT

To model the interaction between the solar wind and the interstellar wind, magnetic fields must be included. Recently Opher et al. 2003 found that, by including the solar magnetic field in a 3D high resolution simulation using the University of Michigan BATS-R-US code, a jet-sheet structure forms beyond the solar wind Termination Shock. Here we present an even higher resolution three-dimensional case where the jet extends for 150AU beyond the Termination Shock. We discuss the formation of the jet due to a de Laval nozzle effect and it's subsequent large period oscillation due to magnetohydrodynamic instabilities. To verify the source of the instability, we also perform a simplified two dimensional-geometry magnetohydrodynamic calculation of a plane fluid jet embedded in a neutral sheet with the profiles taken from our 3D simulation. We find remarkable agreement with the full three-dimensional evolution. We compare both simulations and the temporal evolution of the jet showing that the sinuous mode is the dominant mode that develops into a velocity-shear-instability with a growth rate of $5 \times 10^{-9} \text{ sec}^{-1} = 0.027 \text{ years}^{-1}$. As a result, the outer edge of the heliosphere presents remarkable dynamics, such as turbulent flows caused by the motion of the jet. Further study, e.g., including neutrals and the tilt of the solar rotation from the magnetic axis, is required before we can definitively address how this outer boundary behaves. Already, however, we can say that the magnetic field effects are a major player in this region changing our previous notion of how the solar system ends.

Subject headings: instabilities – interplanetary medium – ISM:kinematics and dynamics – MHD:solar wind – Sun:magnetic fields

1. Introduction

One of the most exciting phenomena in astrophysical media are jets. Usually, they are collimated structures extending for several parsecs near black holes and active galaxies (e.g., Sahayanathan et al. 2003). Recently, we showed (Opher et al. 2003) that due the compression of the solar magnetic field, a jet-sheet structure forms in the region beyond the Termination Shock, where the solar wind becomes subsonic. This structure is narrow and collimated in the meridional plane (jet), but extends in the equatorial plane as a disk for approximately 60° around the upstream direction. This result was obtained using the state-of-the art three dimensional magnetohydrodynamic code (BATS-R-US) with an unprecedented resolution to investigate the region where the solar wind meets the interstellar medium. It was motivated by the approach of the Voyager spacecraft to this region. Voyager is one of the most successful missions of NASA, traveling for more than 25 years with two spacecraft, respectively with a velocity of 3.5AU/year (35° above the ecliptic plane) and 3.1AU/year (48° below the ecliptic plane).

In this section we review the current state of modeling the interaction between the solar and the interstellar wind and discuss why magnetic effects are crucial, especially in the region between the Termination Shock and the Heliopause, the Heliosheath.

Because the solar system travels in the interstellar medium with a velocity of approximately 25km/s (Frisch 1996), the solar wind collides with a supersonic interstellar wind. The basic structures that are formed by this interaction are: the Termination Shock (TS), the Heliopause (HP), and, possibly a Bow Shock (BS). The Termination Shock is the boundary where the supersonic solar wind becomes subsonic slowing down approaching the Heliopause. The Heliopause is the boundary separating the subsonic solar outflow downstream of the Termination Shock and the interstellar plasma flowing around it. The region inside the Heliopause is called the Heliosphere. If the flow of the interstellar wind is also superalvenic, there is a BS further out, where the interstellar flow becomes subsonic to avoid the heliospheric obstacle. In previous hydrodynamic models, the region beyond the Termination Shock has constant plasma pressure and temperature and the heliospheric boundary was a smooth, rounded surface. This is not true if the solar magnetic field is included: the plasma pressure, temperature and density downstream the shock are not uniform and constant, and the heliospheric boundary is highly distorted from the rounded appearance of the hydrodynamic models.

The region between the Termination Shock and the Heliopause, the Heliosheath, is one of the most mysterious and unknown regions. The total plasma beta (the ratio between the sum of the thermal and ram pressure and the magnetic pressure) decreases as one passes through the shock; it is clear that the magnetic field will play a major role in that region (Before the TS, $\beta_{total} \approx 65$. After the TS $\beta_{total} \approx 8$. At the magnetic ridges $\beta_{total} \leq 1 \approx 0.1$). The solar magnetic field reverses polarity at the heliospheric current sheet (HCS). If we neglect the tilt between the solar magnetic and rotation axis, the HCS remains in the equatorial plane. One of the major questions is how the HCS behaves beyond the Termination Shock, or in another words, how the current system in the Heliosphere closes.

The interaction between the solar and interstellar wind is inherently a three dimensional problem because of the magnetic fields. Ideally, modeling this complex region properly would require inclusion of several ingredients: a) the ionized component from the solar and interstellar wind; b) the neutral atoms (coupled to the plasma by charge-exchange collisions); c) the magnetic field (of both the solar wind and the interstellar wind); d) the pickup ions; and e) cosmic rays (both galactic and anomalous components).

For the interstellar wind, we know with certainty neither the magnitude nor the direction of the magnetic field. In the case of the neutral component, the associated particle large mean free path dictates a kinetic treatment. In addition, the diverse length scales present in the problem must be treated consistently (i.e. the numerical resolution of a simulation code must be capable of widely differing resolutions according to the different regions). The scales that we are interested in are on the order of tenths of an AU (for MHD instabilities and the heliospheric current sheet, for example) although the dimensions of the Heliosphere are on the order of a thousand AU. Therefore, another aspect that is important when modeling this interaction is the numerical resolution.

There have been several numerical approaches to tackle this complicated interaction. Much work has focused on the careful treatment of the neutral component. Baranov & Malama (1993, 1995) (see also Baranov, Izmodenov & Malama (1998)) developed a kinetic description for the neutrals using a Monte Carlo approach. These studies, however, neglected magnetic fields. More recently, Baranov & Zaitsev (1995) and Izmodenov, Gruntman & Malama (2001) used the same description and included the interstellar magnetic field in a two dimensional model. Another alternative approach, still in two dimensions and neglecting the magnetic field, was developed by Pauls & Zank (1996) (see also (Zank et al. 1996; Pauls et al. 1995)) who treated the neutrals as an additional fluid species. More recently, Muller, Zank & Lipatov (2000) used a particle-in-mesh approach as a kinetic approximation for the neutrals. Liewer et al. (1996) and Karmesin et al. (1995) used a gasdynamic approach treating the neutrals as a single fluid, also in a two dimensional study. The works by Ratkiewicz et al.

(1998) (see also (Ratkiewicz, Barnes, & Spreiter 2000; Ratkiewicz & McKenzie 2003)) and (Ratkiewicz & Ben-Jaffel 2002) were three-dimensional studies assuming that the neutrals have constant density, velocity and temperature. They also neglected the solar magnetic field and studied the effect of the interstellar magnetic field for several magnitudes and directions.

The works by Pogorolev & Matsuda (2000), McNutt, Lyon & Goodrich (1998), Washimi & Tanaka (1996, 2001) and Linde et al. (1998) were the only ones that included both the solar and interstellar magnetic fields in a self consistent way in three-dimensional treatments. The neutrals were included as a single fluid. The major drawback of these studies are: the inclusion of both of the interstellar and solar magnetic fields and the neutrals making it difficult to differentiate the effect of each component; and the limited spatial resolution.

In our recent study (Opher et al. 2003) we performed a three dimensional study including the solar magnetic field. In order to study how the HCS behaves beyond the TS, we did not include the interstellar magnetic field to eliminate the effect of reconnection between the solar and interstellar fields and to isolate the effect of the solar magnetic field. We used an adaptive mesh refinement allowing us to get to spatial resolutions previously not obtained of the order of 1.5 AU at the HCS. We showed that a *jet-sheet* structure forms at the edge of the solar system. This jet-sheet oscillates up and down due to a velocity shear instability. In that study, we assume as a first approximation that the solar magnetic and the rotation axis are aligned. We also only treat the ionized component and neglect the effect of neutrals. Both effects, i.e., the inclusion of neutrals and the tilt of the dipole, need to be included to assess the overall structure and dynamics of the edge of our solar system. Spatial resolution was a key factor for resolving the jet-sheet structure at the edge of the solar system. We showed that resolutions of the order of 3 AU are insufficient; the jet at the current sheet is broadened and the current sheet remains in the equatorial plane as in the previous studies of Linde et al. (1998); Washimi & Tanaka (1996).

Figure 1 shows the pressure contours of a meridional cut of our simulation with and without the inclusion of the solar magnetic field. The coordinate system is such that the interstellar wind is flowing from the negative x -direction and the solar rotation axis is in the positive z -direction. The run presented in both cases is the *coarse* grid case (see Opher et al. (2003) and Appendix) with resolution of ~ 3 AU at the HCS. It is clear that in the Heliosheath the pressure is not uniform anymore, being enhanced in the region of the current sheet. Also, the HP is more pointed and the distance between the Heliopause and the Bow Shock increases (the HP location moves from 240 AU to 280 AU and the BS location moves from 358 AU to 440 AU), due to the presence of the jet.

In the present study we revisit the work of Opher et al. (2003) in order to study the formation of the jet and the magnetohydrodynamic (MHD) instabilities driven by the jet-

sheet. We present a run where we extended the resolution to 0.75 AU at the HCS. (In the previous study we used a resolution of 1.5 AU at the current sheet, 3-4 times more refined than previous studies.) With such high resolution and extending the refined region, we were able to resolve the jet extending to 150 AU beyond the Termination Shock. We discuss on the effect of the *de Laval* nozzle on the formation of the jet and the width of the jet.

The outline of the paper is the following: In the first section we describe briefly the model (for more details, see Opher et al. (2003)). In the second section, we present our major results for the run used and discuss the effect of the *de Laval nozzle* on formation of the jet. In the third section we discuss the width of the jet. The fourth section is dedicated to the discussion of the role of magnetohydrodynamic instabilities and comparison of the 3D and 2D MHD code. The fifth section is dedicated to the conclusions and discussions. Finally, in the appendix we discuss the dependence of the width of the jet on resolution, showing that at the high resolution case, we obtained grid converged numerical solution.

2. Description of the Model

The code that we are using, BATS-R-US (Block Adaptive Tree Solar wind Roe type Upwind Scheme), was developed at the University of Michigan(Powell et al. 1999). The BATS-R-US code has been designed to capitalize on advances on massive parallel computers; the evolution of adaptive mesh refinement (AMR) techniques and advances in basic numerical methods particularly for hyperbolic conservations laws. The BATS-R-US MHD algorithm uses an upwind methods, approximate Riemann solvers, and limited solution reconstruction (see Powell et al. (1999)). It is a three dimensional magnetohydrodynamic code and the governing equations are the ideal magnetohydrodynamic equations. The resulting finite-volume scheme solves for the hydrodynamic and electromagnetic effects in a tightly coupled matter. It uses block-based solution for the adaptation on a cartesian mesh and is able to have more than 20 levels of refinement. It is a parallel multi-processor code with capability of running in different platforms, such as Beowulf (type PC clusters) and SGI origin 2000 machines.

In this study, as in Opher et al. (2003), we only treat the ionized components neglecting the neutrals. In order to eliminate the effect of reconnection at the heliopause, we did not include an interstellar magnetic field. The inner boundary was chosen at 30 AU and the outer boundary at $3450 \times 4500 \times 4500 \text{ AU}$. The physical boundary conditions are: For the solar wind (at 30 AU): $n_{\text{plasma}} = 7.8 \times 10^{-3} \text{ cm}^{-3}$, $T = 1.6 \times 10^3 \text{ K}$, $v = 450 \text{ km/s}$. The

solar magnetic field at the inner boundary was taken as the Parker spiral magnetic field,

$$\vec{B} = \text{sign}(\cos\Theta) \left[B_0 \left(\frac{R_0}{r} \right)^2 \vec{e}_r - B_0 \left(\frac{R_0^2}{r} \right) \frac{\Omega_\odot \sin\Theta}{u_{sw}} \vec{e}_\phi \right], \quad (1)$$

where R_0 is taken as the inner boundary 30 AU , u_{sw} is the solar wind speed, 450 km/s , Θ is the polar angle of the field line, and Ω_\odot is the equatorial angular velocity of the Sun. At the equatorial plane, $B = B_0 = 2\mu G$. We chose the field polarity ($\text{sign}(\cos\Theta)$) to match the 1996 solar minimum. For the interstellar wind: $n_{\text{plasma}} = 0.07 \text{ cm}^{-3}$, $T = 10^4 \text{ K}$, $v = 25 \text{ km/s}$.

2.1. Jet formation and properties: magnetic ridges and the de Laval nozzle

In the present study we use higher spatial resolutions than the previously reported run (Opher et al. 2003) obtaining a resolution up to 0.75 AU at the current sheet. In the Appendix we comment on the effect of spatial resolution on the width of the jet. In this section, we briefly summarize the major results of this run indicating the major features and differences from the previous case (with resolution of 1.5 AU at the HCS). Figure 2a shows the contours of the magnetic field at $t = 1.3 \times 10^9 \text{ sec}$ (scale ranging from $0 - 0.3 \text{ nT}$). The coordinate system is the same as in Figure 1. Beyond the the Termination Shock (TS), the azimuthal magnetic field is compressed forming *magnetic ridges* (strong field, see region in red). The spatial resolution at the *magnetic ridges* is 3 AU , double of the resolution of previous works (Opher et al. 2003) and the magnetic field intensity ranges from $0 - 0.4 \text{ nT}$ (an increase from 0.24 nT from the previous study). Figure 2b shows the contours of the velocity U_x (in the meridional plane) between the TS and the HP. In both, the black lines, are the flow streamlines.

The velocity of the jet is $\approx 200 \text{ km/s}$ extending for 150 AU beyond the TS, to $x = -320 \text{ AU}$, in the direction of the BS (located at $x = -380 \text{ AU}$). Due to the higher resolution the turbulent vortices are more pronounced (with sizes of $\sim 20 \text{ AU}$) and the structure is more complex than in Opher et al. (2003). The region where the turbulent vortices form has a resolution of $1.5 - 3.0 \text{ AU}$, while the one in Opher et al. (2003) has a resolution of 6.0 AU in the same region (see Appendix for details). The jet is unstable as in Opher et al. (2003). We discuss details of the instability in Section 4.

The jet-sheet structure forms in the region of minimum of magnetic pressure. Figure 2c shows that the flow is in pressure balance after the shock. It portrays the vertical line cut downstream of the TS (at $x = 161 \text{ AU}$), at $y = 0$ for thermal (dashed line), magnetic (dash-dot-dash line) and total (solid line) pressure. Downstream of the shock, where the flow decelerates, conservation of magnetic flux outside of the equatorial plane causes the

field to increase its magnitude further, while in the current sheet there is no such effect. As a result, the increased magnetic field above and below the ecliptic planes effectively pinches the sheet just beyond the Termination Shock, causing the stream lines in the subsonic regions to converge slightly. As pointed out by Washimi & Tanaka (2001), the enhanced magnetic ridges also create an obstacle in the post-shock flow, decelerating and deviating it to the flanks before reaching the Heliopause. This can be seen in Figure 2d where a line cut is taken, 60° above the ecliptic plane. The ram pressure (the green curve) reaches a minimum at the maximum intensity of the magnetic pressure, the *magnetic ridges* (red curve). (See also streamlines in Figure 2a).

Figure 3 shows the ratio of velocity of the jet u with respect to the sound speed a at $t = 1.3 \times 10^9 \text{ sec}$, when the current sheet is still in the equatorial plane (green curve). For comparison, two other cases are presented: the refined (red) and coarse (blue) resolution cases. For the coarse case, the de Laval nozzle effect is negligible due to a broader jet. As we increase the resolution (red curve), the jet extends farther away, in the direction of the Bow Shock. In the refined case (as in Opher et al. (2003)) the jet loses its power at $x = -230 \text{ AU}$ (indicated by the green arrow) while the change in resolution (from 1.5 to 3.0 AU) occurs at $= -320 \text{ AU}$. In the extended case the jet loses its power at $x = -320 \text{ AU}$ (while the BS is at $x = -380 \text{ AU}$, indicated by the red arrow). The change in resolution (0.75 to 1.5 AU) occurs at -350 AU and, from 1.5 to 3.0 AU at -365 AU . This indicates that resolution plays a major role and the jet loses its power due to numerical dissipation.

The converging flow lines near the equatorial plane create a de Laval nozzle: a subsonic flow must accelerate where the streamlines converge and decelerate where flow lines diverge, while the opposite is true for a supersonic flow. Figure 4 shows a schematic drawing of a nozzle along with the streamlines where the jet form. The red arrow indicate the region where acceleration occurs. For a steady gas flow the Euler's equation can be written as (Landau & Lifshitz 1987)

$$\rho v \frac{\partial v}{\partial r} = -\frac{\partial p}{\partial r} + F, \quad (2)$$

where F is the force. Consider a flow of gas through a nozzle with a variable cross section $A(r)$ (as pictured in Figure 4a) Considering the pressure $p = \rho R T$, where R is the gas constant and the mass flux constant $\rho v A(r) = \text{constant}$, the equation above can be written as

$$\frac{v^2 - c_s^2}{v} \frac{dv}{dr} = \frac{T}{\rho} \frac{1}{A} \frac{dA}{dr}. \quad (3)$$

For a narrowing nozzle, $dA/dr < 0$, and the flow velocity increases as long as it is subsonic $v^2 < c_s^2$, reaching a maximum where the cross section is minimum. If the nozzle

then widens again, the flow decelerates thereafter. However, if the flow accelerates sufficiently to become supersonic at the neck, then it will continue to accelerate where the nozzle widens ($dA/dr > 0$). A nozzle that first narrows and then widens again is called the *de Laval nozzle*. This is analogous to what happens in Parker's model of the solar wind at the critical point, where the effective nozzle, created by the combined effects of mass flux conservation and gravity, has a minimum cross section. In the jet formed here, the maximum speed just barely exceeds the sound speed, and decelerates thereafter, much as a breeze in solar wind theory.

At the TS the flow velocity decreases to Mach number 0.55. Due to the acceleration of the flow past the TS, the Mach number increases to 1.1. The velocity of the jet is $\sim 150 \text{ km/s}$ and remains almost constant for the extension of the jet (see Figure 3, where the velocity of the jet decreases only at $x = -320 \text{ AU}$ due to the change in resolution). Fig. 4 shows the location of the *de Laval* nozzle effect.

3. Width of the Jet

What determines the scaling of the width of the jet? Does it depend on the grid resolution at the current sheet? Observations from Pioneer and Voyager indicate that the width of the HCS, at 1 AU is approximately $10,000 \text{ km} = 6.7 \times 10^{-5} \text{ AU}$ (while a surrounding plasma sheet is thicker by a factor of 30 (Smith 2001; Winterhalter et al. 1994)) In terms of proton gyroradius the current sheet thickness is about $200 R_L$ (Winterhalter et al. 1994). For all cases, this is smaller than our grid resolution.

How does the width of the current sheet scales with distance? Neglecting dynamic effects (such as turbulence) and kinetic effects such as drift instabilities, and assuming pressure balance, the width is determined by a balance between the thermal (inside the sheet) and the magnetic pressure outside. Combining the adiabatic energy and the energy equation,

$$(\vec{u} \cdot \vec{\nabla})p + \gamma p(\vec{\nabla} \cdot \vec{u}) = 0 . \quad (4)$$

This equation can be written as

$$u_0 \frac{dp}{dr} + \gamma p \vec{\nabla} \cdot \vec{u} = 0 , \quad (5)$$

where u_0 is the radial solar wind velocity, and r the radial distance from the Sun. Let the width of the current sheet be a , from Eq. (5),

$$\frac{1}{p} \frac{dp}{dr} = \frac{\gamma}{ar} \frac{d(ar)}{dr} \quad (6)$$

that gives the dependence for the thermal pressure with distance as

$$p = (ar)^{-\gamma} , \quad (7)$$

where for an adiabatic gas $\gamma = 5/3$. For a spherical expansion $a \propto r$ and the thermal pressure falls as $r^{-10/3}$. However, since the azimuthal magnetic field falls with distance as r^{-1} , the magnetic pressure falls with r^{-2} . Therefore, from the pressure equilibrium that must exist between the thermal pressure at the current sheet and the magnetic pressure outside the sheet, the dependence of the width with distance must be,

$$a(r) \propto r^{1/5} . \quad (8)$$

Using this scaling, for the observed width of $6.7 \times 10^{-5} AU$ at $1 AU$, the current sheet width at $150 AU$ is $2 \times 10^{-4} AU$ which is much smaller than the grid resolution of our most resolved case.

If the width of the HCS is determined by numerical diffusion, we can estimate the width as follows: For a steady state solution, the induction equation gives the width of the current sheet to be

$$\nabla \cdot (\vec{u} \vec{B} - \vec{B} \vec{u}) = \eta_m \nabla^2 B \quad (9)$$

or approximately

$$\eta_m \frac{B_\phi}{a^2} \approx u_z \frac{B_\phi}{a} , \quad (10)$$

giving the approximately the width as

$$a \approx \frac{\eta_m}{u_z} , \quad (11)$$

i.e., the width of the HCS, a , in steady state, is determined by numerical diffusion η_m and the converging flows to the current sheet. The numerical diffusion η_m will be proportional to the grid spatial resolution. If numerical diffusion determines width, the width decreases as resolution increases. However, this is not observed.

Figure 5a shows the dependence of the jet width on the grid resolution in the region of the current sheet ($-10 AU < z < 10 AU$). Three cases are included: coarse, refined (same as Opher et al. 2003) and the super-refined-extended (the one presented at section 2.1). For the coarse grid, the resolution at the current sheet is $6 AU$, for the refined grid, $1.5 AU$ and for the super-refined-extended grid, $0.75 AU$. The blue and the red curves are, respectively, the half width of the velocity and the magnetic field, measured after the TS, at $x = -210 AU$. The half widths of both the velocity and the magnetic field are measured half way of the maximum. For the three cases, the velocity (jet) profile follows closely the magnetic field (the current sheet) profile, being always slightly broader. As we increase the

resolution at the flanks of the jet, the two profiles approaches each other, almost overlapping. (For more details see Appendix). As we increase the resolution, the width of the velocity (jet) approaches the width of the magnetic field (current sheet). As we increase the resolution, the magnetic field (current sheet) width converges to a value of 4 AU.

Figure 5b presents the the velocity profiles for the three cases: the coarse, the refined and the super-refined-extended cases. The red, green and blue curves, are respectively, the super-refined-extended, refined and coarse cases. The jet is much more resolved at the flanks as well as at the region of the current sheet in the super-refined-extended and the refined cases, compared to the coarse case. The profiles for the velocity for the super-refined-extended and the refined case are almost identical. We can see that the width of the jet, in the super-refined-extended case, is independent of the grid resolution and is determined by the physical conditions, rather than by numerical resolution or numerical diffusion.

4. Instabilities - Comparison of 3D with 2D MHD code

There have been several studies examining magnetized flows in which both sheared flows and sheared magnetic fields are present (Einaudi 1999; Dahlburg, Keppens & Einaudi 2001; Einaudi et al. 2001). A particular configuration studied, motivated by the study of the heliospheric current sheet, was of a fluid jet embedded in a neutral sheet. Studies like Dahlburg, Boncinelli & Einaudi (1998); Einaudi et al. (2001) analyzed the behavior of a plane magnetized jet. Both study were two-dimensional cases (the justification came from laminar nature of the initial system and of the fact that the fastest growing linearly unstable modes are 2D). The configuration studied was a fluid jet in the z direction and the spatial coordinate along which the mean flow varies as y : $\hat{W}_0(y) = \text{sech}(y)\hat{e}_z$ embedded in a neutral sheet $\hat{B}_0 = \tanh(\delta y)\hat{e}_z$, where W_0 and B_0 are the basic velocity field and magnetic field and δ is the magnetic shear width. These studies focus on the response of the wake-neutral or jet-neutral sheet to infinitesimal perturbations. The two unstable modes that exist in the fluid limit (no magnetic field) are the varicose (sausage-like) and sinuous (kink-like) modes. These modes differ in the symmetry of the perturbed velocity component in the direction perpendicular to the flow. For the varicose mode, the perturbed velocity component is antisymmetric in y and, for the sinuous mode it is symmetric. In a magnetically dominated limit, only a tearing mode exists. This mode has the same symmetry as the varicose fluid mode. In the flow-dominated regime the sinuous mode has the fastest linear growth rate (faster than the varicose mode). Both modes are Kelvin-Helmholtz modes of a jet. The sinuous and varicose modes become magnetohydrodynamic modes for finite values of the Alfvén number A , the ratio of the characteristic Alfvén speed to the characteristic flow

speed.

In the 3D case presented in Section 2.1, $v_A \ll 100 \text{ km/s}$ and $v_{flow} \sim 200 \text{ km/s}$ so the Alfvén number, $A \ll 1$. At the location of the jet, there is no magnetic field and we expect the predominant mode to be the sinuous mode. The jet in the 3D case presented in Section 2.1 is unstable and oscillates up and down as in the case presented in Opher et al. (2003), although due to the higher resolution, much more structure can be seen (see attached material for a movie of Figure 2a). Figure 6a presents a measure of the displacement of the current sheet as a function of time. The red curve is the displacement in the middle of the jet, at $x = -225 \text{ AU}$, and the green curve the displacement at the nose, at $x = -290 \text{ AU}$. Indexes (I-III) indicate the different regions of time scales of oscillation. The displacement at the two locations of the jet are anti-correlated, implying that the wavelength of the oscillation λ is $\leq 70 \text{ AU}$. Examining Fig. 6b it is clear that the oscillation is a sinuous mode and that the wavelength is $\lambda \sim 23 \text{ AU}$. There are two distinct time scales. At the beginning of the displacement, a time scale of oscillation of $t_1 = 2 \times 10^8 \text{ sec}$ (region I) and then $t_2 = 2 \times 10^9 \text{ sec}$ (region II). Region III marks the exponential growth of the velocity-shear-Kelvin-Helmholtz instability. The growth rate, measured for curve III is $\Gamma = 5.4 \times 10^{-9} \text{ sec}^{-1}$. (As a comparison, the growth rate measured for the refined case in Opher et al. (2003) was $1.6 \times 10^{-9} \text{ sec}^{-1}$.)

The Kelvin Helmholtz (KH) growth rate, for an infinitely thin layer is (Chandrasekhar 1961) $\Gamma = 0.5 \times |k \cdot U_0| [1 - (2c_A \hat{k} \cdot \hat{B}_0)^2 / (k \cdot U_0)^2]^{1/2}$, where U_0 is the velocity jump across the shear layer, c_A is the Alfvén speed, \hat{k} is the direction of the wavevector (here \hat{x}) and \hat{B}_0 is the direction of the magnetic field. Maximum growth occurs for $k \approx 1/a$, where a is the distance between the maximum velocity and zero. For the 3D run performed here, at $x = -190 \text{ AU}$, $U_0 \approx 150 \text{ km/s}$, and $a \approx 20 \text{ AU}$. With these values the predicted KH growth rate, for planar geometry is $5 \times 10^{-8} \text{ sec}^{-1}$.

To verify that this instability seen in the 3D MHD code is indeed caused by a KH type instability arising in the jet-sheet, we studied a much simpler 2D configuration, analogous to that studied by Einaudi (1999). In our case, the radial magnetic field in the flow direction is negligible, while there is a strong sheared magnetic field perpendicular to this direction. The sheet thickness is much smaller than both the sheet length and its longitudinal extension. Therefore, in the simplified geometry (Bettarini 2003), we model this by considering an initial equilibrium structure in cartesian geometry with velocity V_y that varies in the x direction and is uniform in the y and z directions. The jet-sheet is therefore infinite in the $y - z$ plane. The line profiles for the density, temperature and magnetic field were extracted from the case described in Section 2.1. Figure 7a and 7b presents the initial profiles taken for the velocity of the jet V_{0y} as a function of latitude x and for the magnetic field B_{0z} as a function of the latitude x .

In particular, while in the 3D jet the temperature varies by a factor of almost 10, the density within the jet decreases toward the center by a factor of 3, apart from a small central spike (and corresponding temperature decrease). The initial conditions for the 2D run were therefore chosen to be a uniform density with a higher temperature in the jet, in pressure equilibrium with the transverse magnetic field changing sign in the center of the jet. The code is a 2.5D compressible MHD code which is spectral in one direction (the flow direction y) and uses compact finite differences on a non-uniform grid achieving a spatial resolution of 0.07 AU in the x direction. The overall number of grid points was 130 in the y direction and 128 in the x direction. Non-reflective boundary conditions are imposed in this direction using the method of projected characteristics as in Einaudi et al. (2001). Periodic boundary conditions are imposed on the y direction. (The x and y axes in the 2.5D run correspond, respectively, to the z and x axes in the 3D run.) Initially, the jet-magnetic field equilibrium structure is perturbed by random noise. After an initial transient, the jet develops a sinuous instability, as may be seen by inspecting the density contours shown for different times in Fig. 8. Initially the density is uniform along the jet (the left upper panel). We can see that as the time evolves the jet starts to oscillate in a sinuous mode. Because the jet in this case is of infinite extent, one can not observe the flag-like oscillation involving a total departure from the $z = 0$ axis as seen in the 3D run. Figure 9 shows the growth rate measured by Bettarini (2003). The value obtained is $\Gamma = 5.0 \times 10^9 \text{ sec}^{-1}$ for the maximum wavelength $\lambda = 25 \text{ AU}$. These values are almost identical to what we observe in the 3D runs, for the growth rate and for the λ , which reinforces the idea that the jet oscillation is due to the development of the KH instability.

5. Conclusions and Discussion

In the present study we increase and extend the spatial resolution obtained in Opher et al. (2003) to study in more details the behavior of the jet. The jet-sheet structure is again present and extends for 150 AU beyond the Termination Shock. Turbulent vortices with sizes $\sim 20 \text{ AU}$ are present due to the shear between the jet flow and the surrounding flow being pushed aside. The jet is unstable as in Opher et al. (2003). We show that the a de Laval nozzle occurs at the TS near the current sheet and it is responsible for accelerating the flow to supersonic values after the shock. We address how the width of the current sheet depends on spatial resolution showing that as the resolution increases, the width tend to a finite value of 4 AU . As we increase the spatial resolution, the profiles of the velocity tend to a common shape. This result we believe, indicate that the width of the jet in the high resolution calculation, is independent of the grid resolution, and depends on physical conditions rather than on numerical resolution.

In order to verify and confirm that the instability of the current sheet is a KH type of instability we have also run a 2D compressible MHD case. We used a simple geometry of an infinite jet-magnetic field equilibrium using the profiles for the magnetic field and velocity from our full 3D runs. The jet is unstable and develop a sinuous instability as observed in the 3D run. The growth rate is $5.0 \times 10^{-9} \text{ sec}^{-1}$ in excellent agreement with the value measured in the 3D runs ($5.4 \times 10^{-9} \text{ sec}^{-1}$). The growth rate had a maximum for $\lambda = 25 \text{ AU}$ again in agreement with the λ measured in the 3D runs, 23 AU . This reinforce the idea that the jet oscillation is due to a KH instability.

The presence of the extended jet, turbulence and the magnetohydrodynamic instabilities reinforce the view that the boundary between the solar wind and the interstellar wind is a dynamic environment. It is highly distorted discontinuity and that magnetic effects are a major player in this region. Still other important effects such as neutrals and the tilt of the magnetic axis in respect to the rotation axis need to be included before we can address definitively how this boundary appears. Also, when the interstellar magnetic field is included, reconnection between the solar and interstellar magnetic field will occur.

The inclusion of a tilted heliospheric current sheet very likely will introduce qualitative changes in the picture represented in this paper. Nerney, Suess & Schmahl (1995) investigated analytically the solar cycle imprint on the Heliosheath. They predicted that the 11-year solar cycle would imprint an alternating magnetic polarity envelopes in the Heliosheath. On a much finer scale, there will be strongly mixed polarity regions between the magnetic envelopes due to the reverse magnetic field polarity due to the 25.5-day solar rotation period. The velocity shear instability requires hundreds of years to develop, while the solar magnetic field changes polarity in much shorter time scales. Thus, in order to have a complete picture of the heliosheath, time-dependent boundary conditions on the solar magnetic field need to be included. By the picture described in this paper, we expect however, that this region will be very turbulent and dynamic.

The *Voyager* spacecraft is now at $\approx 85 \text{ AU}$ and is approaching the Termination Shock (there is current controversy on whether it already encounter it (Krimigis et al. 2003; McDonald et al. 2003)). *Voyager* travels 35° above the ecliptic plane towards the nose of the heliosphere. We expect that *Voyager* will encounter an extremely turbulent dynamic region that will have a major effect in the energetic particle detected by the instruments on *Voyager*.

Finally, for other magnetized rotating stars in motion with respect to the interstellar medium we expect to find similar phenomena. We expect the presence of an extended jet or disk with length of $\sim 150 \text{ AU}$ and a width of 10 AU beyond the location where stellar winds are shocked in respect to the interstellar medium that surround them.

This work is a result of the research performed at the Jet Propulsion Laboratory of the California Institute of Technology under a contract with NASA. The University of Michigan work was also supported by NASA. GT was partially supported by the Hungarian Science Foundation (OTKA, grant No. T037548). We thank F. Rappazzo and S. Landi for useful discussions.

APPENDIX: DEPENDENCE OF THE WIDTH OF THE JET ON SPATIAL RESOLUTION

In this appendix we present the grids for the three cases. Figure 10-12 show the contours of the azimuthal magnetic field B_y for the coarse, refined and super-refined-extended cases. The red lines indicate the change in the grid resolution. The numbers indicate the resolution in each region, in AU . For the coarse grid, the resolution between the TS and the HP, at the HCS, is $6.0 AU$. For the refined grid, the resolution between the TS and HP, at the HCS, is $1.5 AU$. In the super-refined-extended case the resolution between the TS and HP, at the HCS, is $0.75 AU$.

Figure 13 shows the magnetic field (solid line) and the velocity profiles (dashed line) for the super-refined extended case. Notice that the magnetic field profile is inverted. We can see how the flow profile adjust itself to the magnetic one. For the three cases the flow profile is broader than the magnetic one. As we increase the resolution, the two profiles almost overlap, and the width of the jet is shaped by the HCS width.

REFERENCES

Baranov, V. B., & Malama, Y.G. 1993, J. Geophys. Res., 98, 15157.

Baranov, V. B., & Malama, Y.G. 1995, J. Geophys. Res., 100, 14755.

Baranov, V. B., & Zaitsev, N. A. 1995, Astron. Astrophys. 304, 631.

Baranov, V. B., Izmodenov, V. V., & Malama, Y. G. 1998, J. Geophys. Res., 103, 9575.

Bettarini, L. 2003, University of Florence, M.A. Thesis.

Chandrasekhar, S., 1961, *Hydrodynamic and Hydromagnetic Stability*, (Clarendon, Oxford, England).

Dahlburg, R.B., Boncinelli, P., & Einaudi, G. 1998, Phys. Plasmas, 5, 79.

Dahlburg, R.B., Keppens, R., Einaudi, G. 2001, Physics. Plasmas, 8, 2001.

Einaudi, G., 1999, Phys. Control. Fusion, A293, 41.

Einaudi, G., Chibbaro, S., Dahlburg, R. B., & Velli, M. 2001, ApJ, 547, 1167.

Frisch, P. C. 1996, Space Sci. Rev., 78, 213.

Izmodenov, V., Gruntman, M., & Malama, Y. G. 2001, J. Geophys. Res., 106, 10681.

Krimigis, S.M., Decker, R.B., Hill, M.E., Armstrong, T.P., Gloecker, G., Hamilton, D.C., Lanzerotti, L.J., & Roelof, E.C. 2003, Nature, 426, 45.

Landau, L.D., & Lifshitz, E. M. 1987, Fluid Mechanics (Oxford: Pergamon)

Liewer, P.C., Karmesin, S.R., & Brackbill, J.U. 1996 J. Geophys. Res., 101, 17119.

Karmesin, S.R., Liewer, P.C., & Brackbill, J.U. 1995 Geophys. Res. Lett., 22, 1153.

Linde, T.J., Gombosi, T.I., Roe, P.L., Powell, K.G., & DeZeeuw, D.L. 1998, J. Geophys. Res., 103, 1889.

McDonald, F.B., Stone, E.C., Cummings, A.C., Heikkila, B., Lai, N., & Webber, W.R. 2003, Nature, 426, 48.

McNutt Jr., R.L., Lyon, J., & Goodrich, C. C. 1998, J. Geophys. Res., 103, 1905.

Muller, H-R, Zank, G.P., & Lipatov, A.S. 2000, J. Geophys. Res., 105, 27419.

Nerney, S., Suess, S.T., & Schmahl, E.J. 1991, AA, 250, 556.

Nerney, S., Suess, S.T., & Schmahl, E.J. 1995, J. Geophys. Res., 100, 3463.

Opher, M. Liewer, P. C., Gombosi, T. I., Manchester, W., DeZeeuw, D. L., Sokolov, I., & Toth, G. 2003, ApJ, 591, L61.

Parker, E. N. 1958m ApJ, 123, 644.

Pauls, H.L., Zank, G.P., & Williams, L.L. 1995, J. Geophys. Res., 100, 21595.

Pauls, H.L., & Zank, G.P. 1996, J. Geophys. Res., 101, 17081.

Pogorolev, N.V., & Matsuda, T. 2000, A&A, 354, 697.

Powell, K.G., Roe, P.L., Linde, T.J., Gombosi, T.I., and DeZeeuw, D.L. 1999, J.Comput.Phys., 154, 284.

Ratkiewicz, R., Barnes, A., Molvik, G. A., Spreiter, J. R., Stahara, S. S., Vinokur, M., Venkateswaran, S. 1998, *Astron. & Astrophysics*, 335, 363.

Ratkiewicz, R., Barnes, A., & Spreiter, J. R. 2000, *J. Geophys. Res.*, 105, 25021.

Ratkiewicz, R., & McKenzie, J. F. 2003, *J. Geophys. Res.*, 108, 6.

Ratkiewicz, R., & Ben-Jaffel, L. 2002, *J. Geophys. Res.*, 107, 2.

Sahayanathan, S., Misra, R. & Kembhavi, A. K. 2003, *ApJ*, 588, 77.

Smith, E. J. 2001, *J. Geophys. Res.*, 106, 15819.

Suess, S.T. 1990, *Rev. Geophys.*, 28, 97.

Washimi, H., & Tanaka, T. 1996, *Space Sci. Rev.* 78, 85.

Washimi, H., & Tanaka, T. 2001, *Adv. Space Res.*, 27, 509.

Winterhalter, D., E.J. Smith, E. J., Burton, M. E., Murphy, N., & McComas, D. J. 1994, *J. Geophys. Res.*, 99, 6667.

Velli, M. 1994, *ApJ*, 432, L55.

Zank, G.P., Pauls, H.L., Williams, L.L., & Hall, D. T. 1996, *J. Geophys. Res.*, 101, 21639.

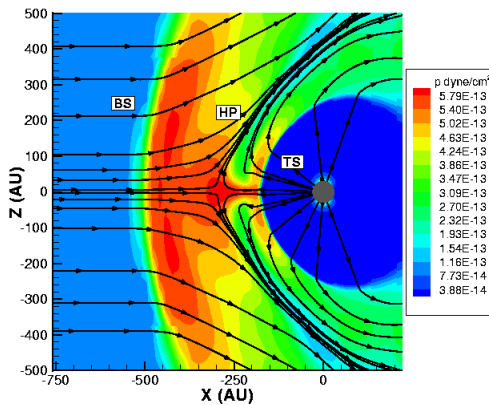
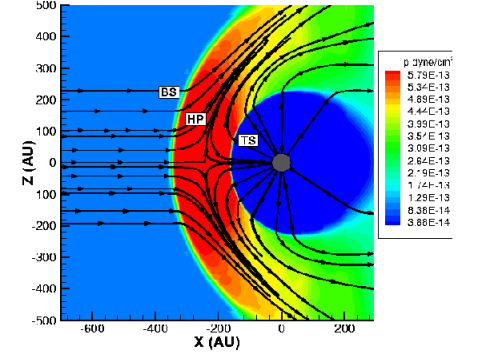
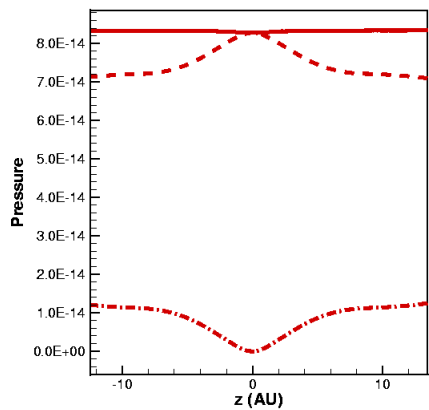
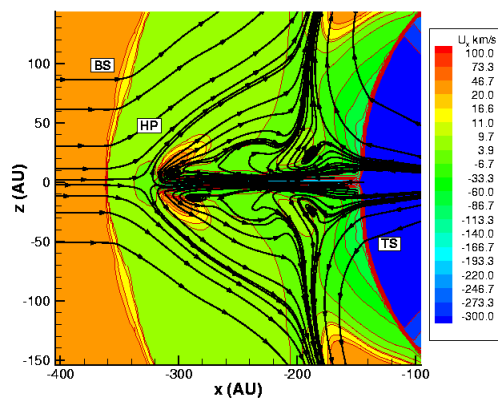
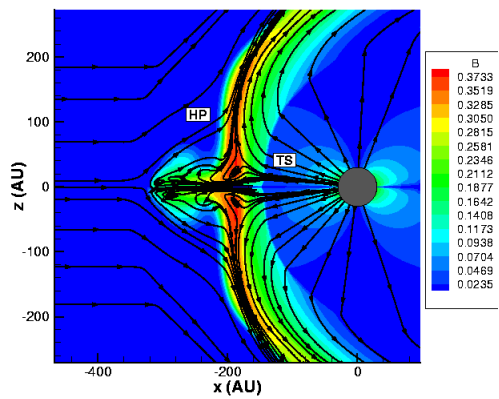


Fig. 1.— (a) Contours of pressure at $t = 1.0 \times 10^9$ sec in the meridional plane (x-z) without the solar magnetic field. Same as (a) but with the solar magnetic field. The case presented here is the *coarse* case, with resolution of the grid at the current sheet of $\sim 3AU$.



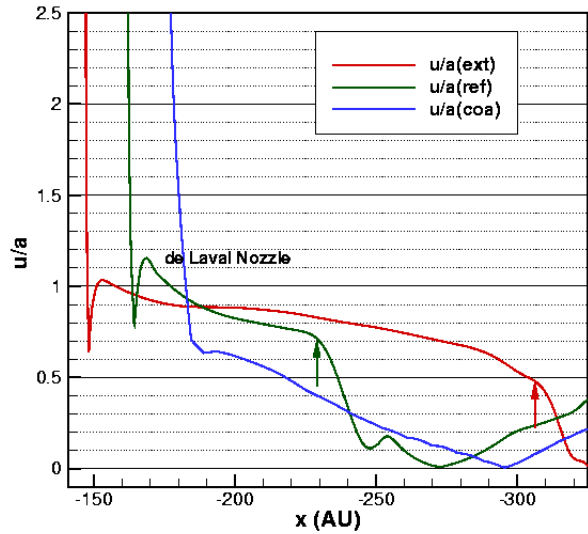


Fig. 3.— Line plot of the equatorial cut at $t = 1.5 \times 10^9$ sec of the ratio velocity per sounds speed a vs. x . Three cases are shown: super-refined-extended (red), refined (green) and coarse (blue). The green and blue refers to the cases at Opher et al. 2003. As we increase the resolution the jet(red) extends farther away. The de Laval nozzle is still present. The refined jet (green) lose its power at $x = -230$ AU (indicated by the green arrow), while the change in resolution from 1.5 to 3.0 AU occurs at $x = -320$ AU. The extended jet (red) lose its power at $x = -320$ AU (indicated by the red arrow) while the change in resolution (from 0.75 to 1.5 AU at $x = -350$ AU and from 1.5 to 3.0 AU at $x = -365$ AU.

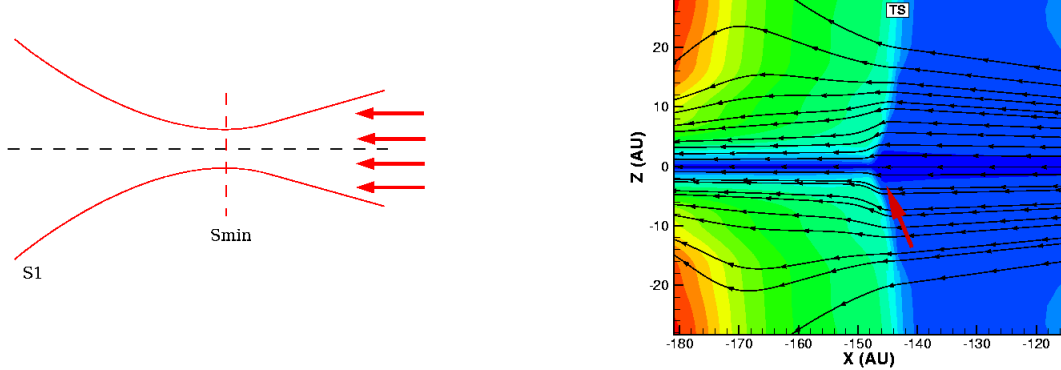


Fig. 4.— (a) Schematic drawing illustrating the formation of the *de Laval Nozzle*. (b) Close view of the region of the *de Laval* nozzle just after the TS. The red arrow indicate the *de Laval* nozzle, where the flow converges.

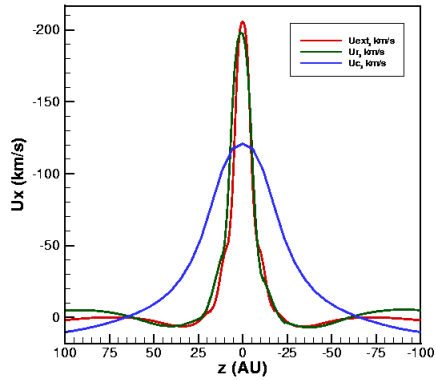
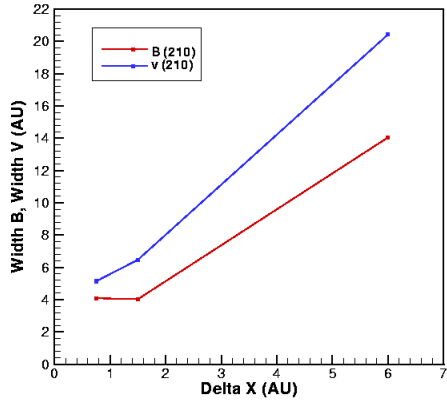


Fig. 5.— (a) Width of the current sheet and the jet vs resolution measured at $x = -210AU$. The red line is the magnetic field width and the blue line is the velocity width
(b) Velocity profiles for the coarse, refined and super-refined-extended cases.

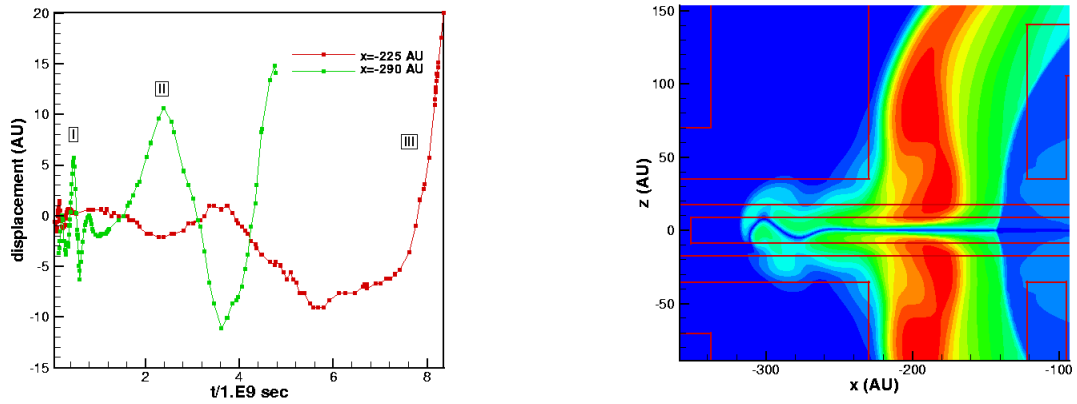


Fig. 6.— (a) Displacement of the current sheet (AU) vs $t/10^9 \text{ sec}$ for $x = -225 \text{ AU}$ (red) and $x = -290 \text{ AU}$ (green). Indexes (I)-(III) marks the different regions of time scales of oscillation. (b) Contours of the magnetic field at $t = 16.8 \text{ years}$. The scale is the same as Fig2a.

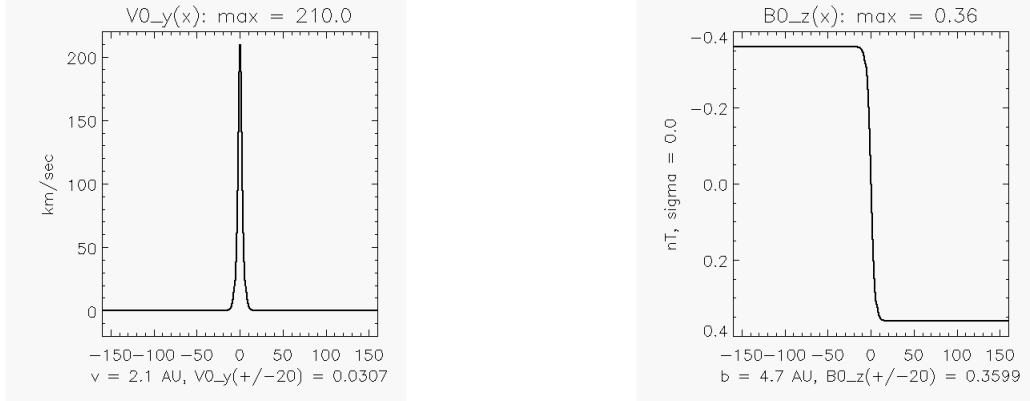


Fig. 7.— (a) Initial profile for the velocity of the jet $V0_y$ as a function of latitude x for the 2D simulations. (b) Initial profile for the magnetic field $B0_z$ as a function of the latitude x .

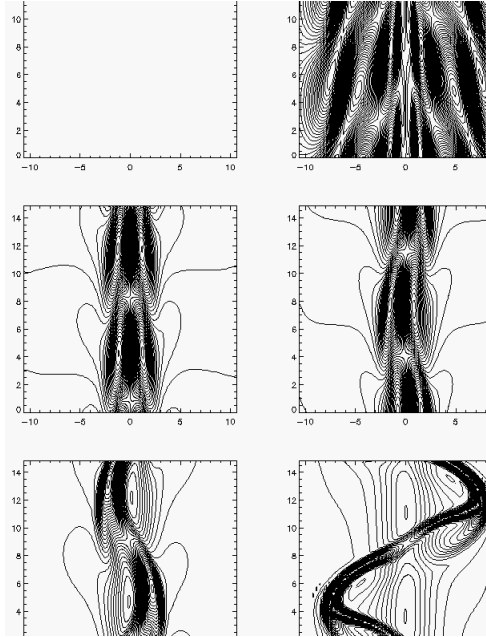


Fig. 8.— Density contours for the 2D compressible MHD run in the xy coordinate system.

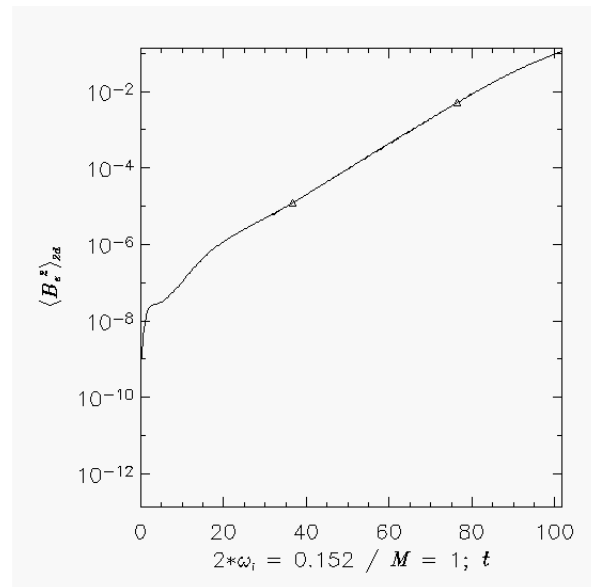


Fig. 9.— Displacement of the current sheet vs t for the 2.5D compressible MHD run.

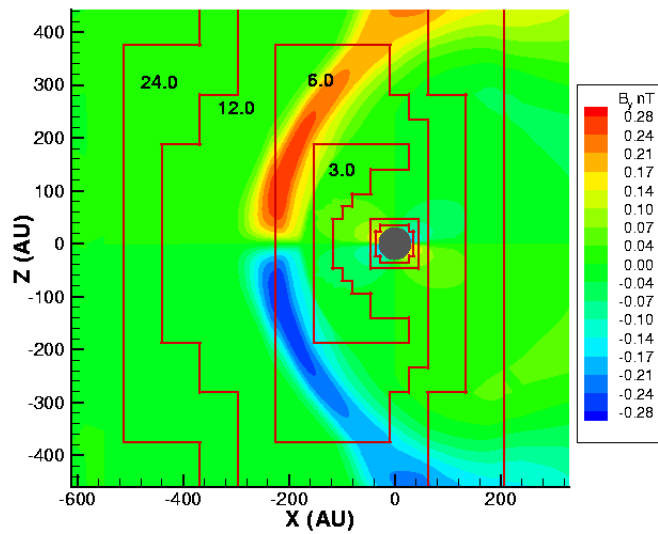


Fig. 10.— The contours of the azimuthal magnetic field, B_y , for $t = 10^9$ sec for the coarse case. The red lines indicate the changes in grid resolution. The numbers indicate the grid resolution (in AU).

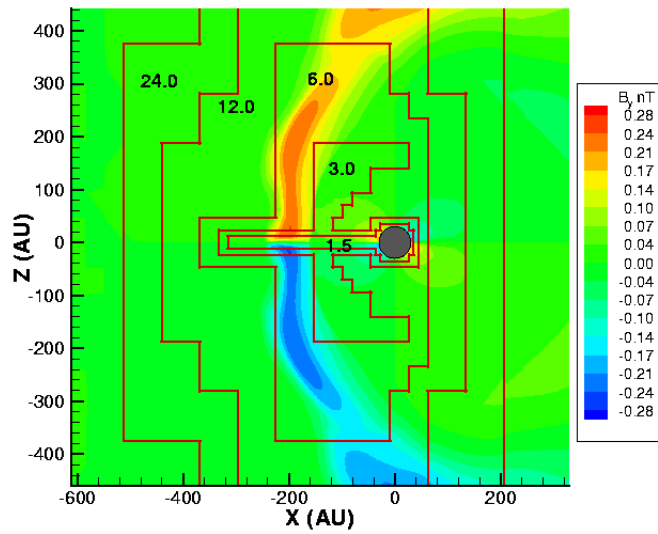


Fig. 11.— The contours of the azimuthal magnetic field, B_y , for $t = 10^9$ sec for the refined case. The red lines indicate the changes in grid resolution. The numbers indicate the grid resolution (in AU).

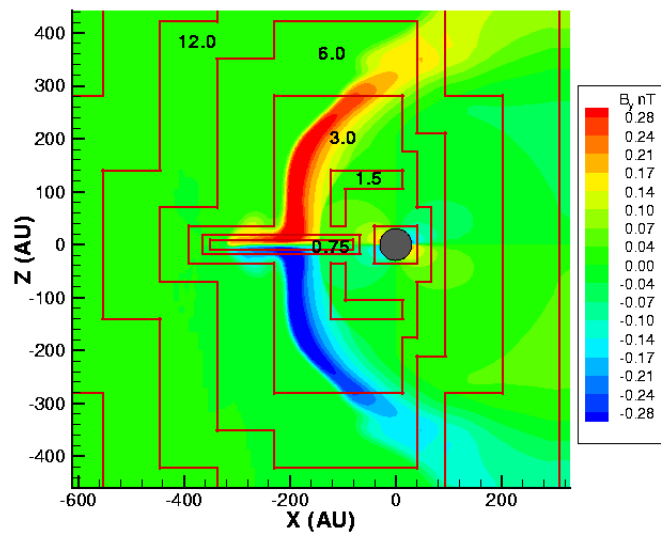


Fig. 12.— The contours of the azimuthal magnetic field, B_y , for $t = 10^9$ sec for the super-refined-extended case. The red lines indicate the changes in grid resolution. The numbers indicate the grid resolution (in AU).

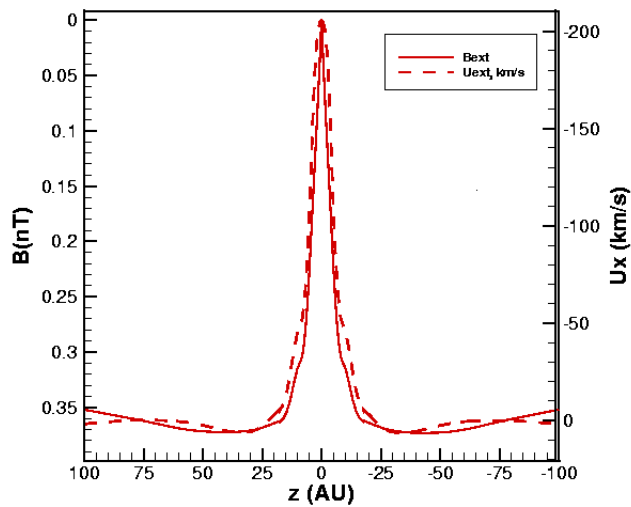


Fig. 13.— Velocity and magnetic field profiles for the super-refined-extended case. The full line is the magnetic field and the dashed line is the velocity profile. Note that the magnetic field profile is inverted.